


Dispersion Morphing in Stretchable Rotator Lattices

Lezheng Fang¹ and Michael J. Leamy^{1*}

School of Mechanical Engineering, Georgia Institute of Technology, Atlanta, Georgia 30332, USA

 (Received 18 May 2023; revised 26 July 2023; accepted 5 September 2023; published 25 September 2023)

Using analytical and numerical means, we document a geometry-enabled phenomenon, termed herein *dispersion morphing*, in which lattice stretching in rotator structures modifies the real and imaginary dispersion characteristics of the system. We then demonstrate diverse functionality derived from dispersion morphing under adiabatic (static) and nonadiabatic (dynamic) lattice deformation, to include dramatic changes in group velocity, refractive index, directivity, and amplification. The proposed rotator lattices consist of in-plane rotators coupled by angled elastic linkages the location and spacing of which can be easily reconfigured, allowing significant changes in the dispersion characteristics of the lattices. Under adiabatic lattice deformation, we reconfigure the directivity and refractive index of the periodic structure and present a closed-form solution to achieve flat bands across the entire wave-number domain. We also incorporate chirality in the unit-cell design to counteract pass-band shifting in the process of dispersion morphing, such that a real-time wave manipulation becomes possible. For dynamic lattice deformation, we model the lattice constant as (i) a step function of time and (ii) a harmonic function of time. In the former scenario, we employ the concept of temporal interfaces and achieve on-demand time delay of the propagation. In the latter scenario, we demonstrate a parametric amplification effect with stretching-informed amplification parameters. We report strong agreement between our theoretical analysis and numerical simulations, verifying the aforementioned findings. We believe that the versatile adaptations of such rotator lattices and their rich dynamics may inspire next-generation reconfigurable and multifunctional metamaterial devices.

DOI: [10.1103/PhysRevApplied.20.034057](https://doi.org/10.1103/PhysRevApplied.20.034057)

I. INTRODUCTION

Elastic metamaterials are a class of structures engineered with (typically) periodic arrays of unit cells exhibiting unique mechanical properties not commonly found in nature [1,2]. In the field of wave propagation, elastic metamaterials have been found to exhibit exotic phenomena, such as negative refraction [3–5], on-demand waveguiding [6–9], band-gap-based filtering [10–13] and topological protection [14,15], making them promising candidates for vibration-control applications [16,17] and mechanical-logic devices [18–20]. The key mechanism governing the diverse forms of wave behavior is the dispersion relationship(s) induced by the spatial periodicity of the lattice and, in some cases, its combination with external modulation.

A conventional metamaterial design approach aims to tailor the band structure of a material for a single purpose. However, when the operating environment or the demanded propagation pattern changes, redesign and fabrication become imperative. This necessity raises concerns about the efficiency and cost-effectiveness of elastic metamaterials. In recent years, there has been a growing demand for metamaterials with reconfigurable band

structures, which adapt to diverse operating environments without incurring excessive modifications or additional costs. A typical active approach to enhance reconfigurability is to include electrical components, e.g., piezoelectric or electromagnetic devices, to modify material properties and thus the dispersion. This approach relies on externally programmed controls and enables reconfigurable frequency filtering [21–23] and interface and/or domain relocation [24–26]. When external controls are restricted or not desired, passive methods leveraging nonlinearity provide moderate tunability in dispersion. In lattice structures with monotonic nonlinear interactions, the dispersion curves shift in frequency and/or wave number [27], enabling pass-band extensions and amplitude filters [28]. In nonmonotonic nonlinear interactions, nonlinearity usually induces bistable or multistable equilibria, with distinct band structures associated with each state. The band-structure reconfiguration has been activated using spring deformation [29,30], buckling [31–33], origami-based deformation [16], and liquid capillarity [34]. However, these systems typically only allow transitions between a few distinct stable states, limiting the degree of reconfigurability and thus applicability.

In this study, we propose a class of stretchable rotator lattices with large continuous reconfigurability enabling

*michael.leafy@me.gatech.edu

multifunctional applications. The stretchable lattices contain an infinite number of stable equilibrium states with smooth dispersion transitioning. We term this phenomenon *dispersion morphing*. We pay particular attention to two rotator designs utilizing rotational geometry, the unit cells of which can be described as either symmetric or chiral. The symmetric type represents a significant advance over previous rotator-lattice designs [35,36] due to generalizations of the rotational geometry (i.e., the coupling position and unit-cell spacing). Meanwhile, our chiral type amounts to a rotator-lattice class that has not previously been studied, which we employ to achieve real-time wave steering, a feature only sparsely explored in the literature [37,38]. In Sec. II, we provide a detailed description of the two types of rotator lattices, with a particular emphasis on their morphed dispersion due to geometry changes. Lastly, in Secs. III and IV, we implement adiabatic and nonadiabatic lattice stretching in numerical simulations and study anomalous wave-propagation patterns. These studies suggest diverse applications for the proposed multifunctional rotator lattices with the potential to inspire new wave-based devices.

II. LATTICE DESIGN

We next present the system descriptions of symmetric rotator lattices (SRLs) and chiral rotator lattices (CRLs), respectively. In the scope of this study, we investigate both adiabatic (static) and nonadiabatic (dynamic) lattice stretching. The lattice constant and equivalent torsional stiffnesses are defined as functions of time. The dispersion analysis presented in this section focuses on the effects of geometry variation under adiabatic conditions. The analysis associated with nonadiabatic conditions is presented in Sec. IV. The system parameters are adapted from our previous experiment on rotator lattices [36] and have been normalized for the sake of clarity and presentation.

A. Symmetric rotator lattice

Figure 1(a) illustrates a 1D monatomic rotator lattice wherein each rotator is pinned to an axis at its center and connected to its neighbors by two pairs of pretensioned springs. This structure exhibits up-down symmetry and is therefore termed the symmetric rotator lattice (SRL). In each unit cell, we define the rotational inertia I , spring stiffness k_s , undeformed spring length L_s , arm length r , and offset angle β_0 . The offset angle β_0 describes the orientation of arms with respect to the vertical direction (perpendicular to the lattice direction). The spacing between rotators (measured from center to center), and thus the lattice constant $a(t)$, may be prescribed through static or dynamic stretching. Appendix A details one design for doing so in a 1D chain. In the following analysis, we define a normalized lattice constant, $\alpha(t) \equiv a(t)/r$. We note that the two

rotator lattices examined in previous work [36] correspond to two special cases of this generalized model with $\beta_0 = 0$ rad and $\beta_0 = \pi/2$ rad and with no time dependence in the lattice constant.

To characterize the SRL dynamics, we introduce the angular displacement θ_j (with counterclockwise rotation being positive) for the j th rotator relative to the horizontal positive direction [the black dashed line in Fig. 1(b)]. The governing equation of motion for the SRL unit cell is nonlinear due to the rotational geometry. In the scope of this study, we confine our attention to the propagation of small-amplitude waves and isolate the linear terms from higher-order terms by expanding the equation of motion around the stable equilibrium $\theta_j = 0$,

$$I\ddot{\theta}_j + \epsilon(2K_{1s}(t)\theta_j + K_{2s}(t)\theta_{j-1} + K_{2s}(t)\theta_{j+1}) + O(\epsilon^2) = 0, \quad (1)$$

where ϵ denotes a bookkeeping device tracking the order of each term in the Taylor expansion; it can be set to 1 in subsequent numerical-integration studies. The equivalent linear torsional stiffnesses $K_{1s}(t)$ and $K_{2s}(t)$ depend on the spring parameters (k_s and L_s) and the rotational geometry (r , $\alpha(t)$, β_0). The explicit expressions for these equivalent stiffnesses take cumbersome forms. For sake of brevity, we document the general forms in Appendix B.

Adiabatic lattice stretching suggests a lattice deformation much slower than the wave dynamics such that the dispersion relationship is assumed to be static and corresponds to each value of the equivalent stiffnesses during their evolution. Hence, we drop the time dependence in all parameters for adiabatic analysis. Applying the Bloch theorem [39] to Eq. (1) yields the linear (static) dispersion relationship,

$$\omega = \pm \sqrt{\frac{1}{I}(2K_{1s} + 2K_{2s} \cos \mu)}, \quad (2)$$

where ω and μ denote the SRL frequency and dimensionless propagation constant, respectively. Conventionally, we consider the positive frequency only. The propagation constant is a nondimensional quantity, the range of which in the first Brillouin zone remains fixed from $-\pi$ to π regardless of changes in the lattice constant. For later graphical illustration, we evaluate Eq. (2) using a set of normalized system parameters presented in Table I.

As such, we present a series of dispersion curves in Fig. 1(c) corresponding to various offset angles at a value of α equal to 2.8. At $\beta_0 = 0$ rad, the SRL exhibits an acoustic dispersion curve similar to that of a conventional rectilinear monatomic chain. With increasing values of β_0 , the dispersion curve deviates from the acoustic branch and gradually morphs toward a flat band. At approximately $\beta_0 = 0.96$ rad, the dispersion curve flattens out

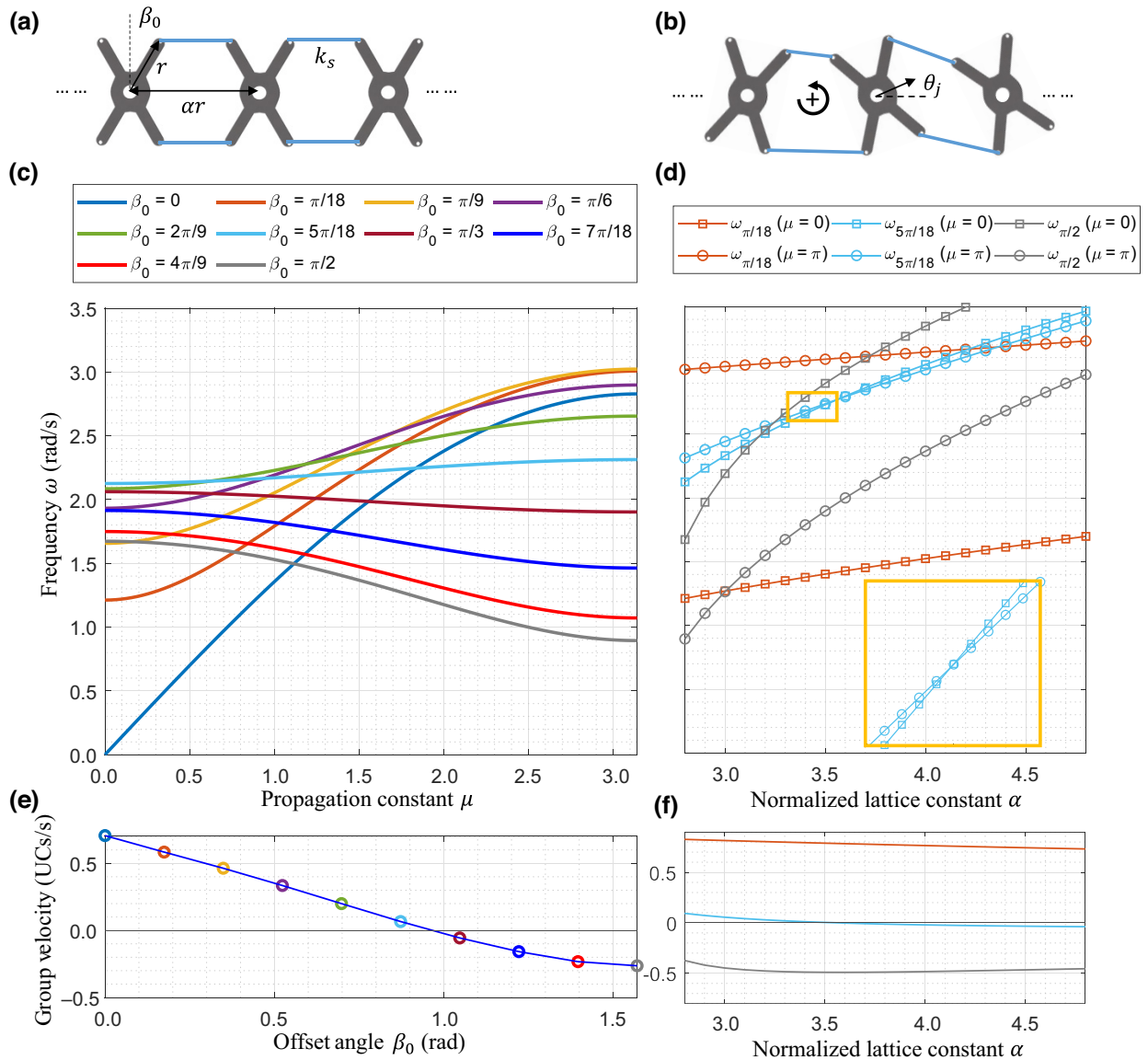


FIG. 1. (a) A schematic of a one-dimensional (1D) symmetric rotator lattice (SRL) in its equilibrium position. The blue segments represent elastic springs. (b) A schematic of the 1D SRL during motion. (c) Dispersion curves at different offset angles. (d) The cut-on and cut-off frequencies at different normalized lattice constants. The inscribed plot magnifies the orange highlighted region. (e) The group velocity at $\mu = \pi/2$ for each offset angle [the marker colors match the dispersion curves in (c)]. (f) The group velocity at $\mu = \pi/2$ for each dispersion relation presented in (d).

across the entire wave-number domain. This emergence of the flat band can be attributed to the elimination of the equivalent torsional linear stiffness, $K_{2s} = 0$, indicating that the rotators are decoupled from one another in the linear regime, thus creating an acoustic vacuum [40]. Although higher-order interactions may exist, this configuration prevents the propagation of Bloch waves and exhibits pronounced energy-localization effects. Beyond this critical offset angle, the dispersion curve undergoes a transition from a positive-group-velocity branch to a negative-group-velocity branch, which effectively alters the sign of the relative refractive index according to Snell's

law [41]. We define the group velocity as

$$c_g = \frac{d\omega}{d\mu} = -\frac{K_{2s} \sin(\mu)}{I\omega}, \quad (3)$$

where c_g quantifies the velocity of energy propagation in units of “unit cells (UCs) per second.” We purposely avoid describing it using m/s , which factors in the lattice constant, since the lattice constant is subject to change due to stretching. Figure 1(e) illustrates the evolution of the group velocity at $\mu = \pi/2$ with respect to an increasing

TABLE I. The SRL parameters.

Parameter	Value
I (kg m ²)	1
r (m)	1
k_s (N/m)	1
L_s (m)	0.6

offset angle. The horizontal intercept locates the flat band discussed above.

In addition to examining the effects of the offset angle on the dispersion relationship, it is of great interest to investigate the impact of adiabatic lattice stretching at fixed offset angles, which mimics an acoustoelastic effect. Note that we assume linearly elastic springs and uniform deformation at all times. In Fig. 1(d), we describe the evolution of cut-on and cut-off frequencies at $\beta_0 = \pi/18, 5\pi/18$, and $\pi/2$, as functions of the lattice constant. We note that since the dispersion relation defined in Eq. (2) is a monotonic function, the cut-on and cut-off frequencies fully define the range of the pass band. At $\beta_0 = \pi/18$ and $\pi/2$, both the cut-on and cut-off frequencies increase with an increasing lattice constant, indicating an up-shifting pass band. The curves representing the cut-on and cut-off frequencies do not intersect in the range shown for α . At $\beta_0 = 5\pi/18$, however, the increasing cut-on and cut-off frequencies meet at $\alpha = 3.65$ and switch thereafter, suggesting the emergence of a flat band. This phenomenon is also captured in Fig. 1(f), where the group-velocity curve crosses the horizontal axis. By setting $K_{2s} = 0$, we derive this critical lattice constant α^* ,

$$\alpha^* = \frac{\sin(\beta_0)(4r \sin^2(\beta_0) + L_s \sin(\beta_0) - 2r)}{r(2 \sin^2(\beta_0) - 1)}. \quad (4)$$

We note that a critical lattice constant only applies if the offset angle β_0 exceeds $\pi/4$. In cases where the offset angle is smaller than $\pi/4$, stretching the lattice will not generate a flat band. Conversely, Eq. (4) can be rearranged to yield a critical offset angle, $\beta_0^* \in (\pi/4, \pi/2]$, at a finite normalized lattice constant α .

Thus, we demonstrate that modifying either the offset angle or the lattice constant under adiabatic conditions can independently induce morphing of the dispersion curves of the system into a flat band and thus cause a reversal in the sign of the group velocity. Contrasting the morphed dispersion curves in Figs. 1(c) and 1(d) reveals that the reconfiguration of the offset angle morphs the dispersion curves at a relatively constant frequency range, whereas reconfiguration of the lattice constant significantly up-shifts and narrows the pass band.

B. Chiral rotator lattice

An alternative approach for constructing a 1D rotator lattice is to incorporate chirality with asymmetric

couplings along the lattice direction. We depict a 1D CRL at its equilibrium position in Fig. 2(a), where we connect neighboring rotators with pretensioned springs (of stiffness k_c and undeformed length L_c) on alternating sides of the rotator chain. This serpentine connection represents a chiral pattern in which adjacent rotators form pairs of enantiomers. We denote the lattice spacing by $\alpha(t)$ and a non-negative compromising angle by $\beta(t)$. We show in later analysis that this compromising angle $\beta(t)$ is a function of the prescribed lattice spacing $\alpha(t)$. In addition to the spring linkages, to maintain equilibrium, each rotator is subject to an external torque applied from its base. These torques, illustrated as black arrows, have constant magnitude, Γ_0 , and alternating directions from one unit cell to another,

$$\Gamma_j = (-1)^j \Gamma_0. \quad (5)$$

In practice, these constant torques can be delivered by devices such as circular-patterned beams [42].

We define the angular displacement at each rotator, θ_j , from its equilibrium position, as depicted in Fig. 2(b), and consider counterclockwise displacement as the positive direction. We then derive the governing equation of motion of the CRL for small angles,

$$I\ddot{\theta}_j + K_0(t) + \epsilon(2K_{1c}(t)\theta_j + K_{2c}(t)\theta_{j-1} + K_{2c}(t)\theta_{j+1}) - \Gamma_j + O(\epsilon^2) = 0, \quad (6)$$

where $K_{1c}(t)$ and $K_{2c}(t)$ are equivalent torsional stiffnesses with explicit forms documented in Appendix B. The dc term $K_0(t)$ arises as a torque from the pretensioned asymmetric springs,

$$K_0(t) = (-1)^j 2k_c r \delta(t) \cos \beta(t), \quad (7)$$

where the spring deformation $\delta(t)$ takes the form of

$$\delta(t) = \alpha(t)r - L_c - 2r \sin \beta(t). \quad (8)$$

Similar to those in an SRL, under adiabatic lattice stretching, the stretch-induced changes in these stiffness terms can be treated statically when compared to the wave dynamics. We thus drop the time dependence of the system parameters in the following analysis.

Since $\theta_j(t)$ is defined from the equilibrium position, the dc terms $K_0 - \Gamma_j$ in Eq. (6) cancel out at the equilibrium position, yielding

$$2k_c r (\alpha r - L_c - 2r \sin \beta) \cos \beta - \Gamma_0 = 0, \quad (9)$$

which can be rearranged to derive the compromising angle as a function of the lattice constant, $\beta(\alpha)$. It is convenient to evaluate this function numerically. Using the

TABLE II. The CRL parameters.

Parameter	Value
I (kg m ²)	1
r (m)	1
k_c (N/m)	2
L_c (m)	2
Γ_0 (Nm)	0.4

parameter in Table. II, we describe the evolution of $\beta(\alpha)$ and the associated spring elongation $\delta(\alpha)$ under adiabatic lattice stretching in Fig. 2(c).

This illustration suggests that both the compromising angle and the spring elongation rise when the lattice constant increases adiabatically. In fact, the lattice stretching primarily affects the compromising angle β until the angle approaches its limit, $\pi/2$, after which we observe a rapidly increasing spring deformation. Figure 2(d) provides the resultant equivalent torsional stiffnesses.

With the dc terms removed and time dependence dropped, we simplify Eq. (6):

$$I\ddot{\theta}_j + \epsilon(2K_{1c}\theta_j + K_{2c}\theta_{j-1} + K_{2c}\theta_{j+1}) + O(\epsilon^2) = 0. \quad (10)$$

We then solve for the (static) dispersion relationship and the group velocity of a CRL:

$$\omega = \pm\sqrt{\frac{1}{I}(2K_{1c} + 2K_{2c}\cos\mu)}. \quad (11)$$

$$c_g = \frac{d\omega}{d\mu} = -\frac{K_{2c}\sin(\mu)}{I\omega}. \quad (12)$$

In Figs. 2(e) and 2(f), we observe a similar phenomenon in which the lattice stretching morphs the dispersion curve from a positive-group-velocity one to a flat band and then a negative-group-velocity one. Different from the SRL, the pass bands in the CRL maintain approximately the same frequency band ($\omega = 1.5$ rad/s) until much larger stretching shifts the pass band upward. This phenomenon can be explained by Eq. (11) and the stiffness evolution depicted in Fig. 2(d). We use the center frequency at $\mu = \pi/2$ to represent the location of each band. According to Eq. (11), the center frequency, $\omega(\mu = \pi/2) = \sqrt{2K_{1c}/I}$, is proportional to $\sqrt{K_{1c}}$. This value, as illustrated in Fig. 2(d), varies slowly with increasing stretching until $\alpha = 4.2$, when it starts to increase, matching the observation of pass-band shifts in Fig. 2(f). Hence, we demonstrate that the dispersion morphing in the CRL avoids excessive pass-band shifts observed in the SRL at low and medium levels of lattice stretching.

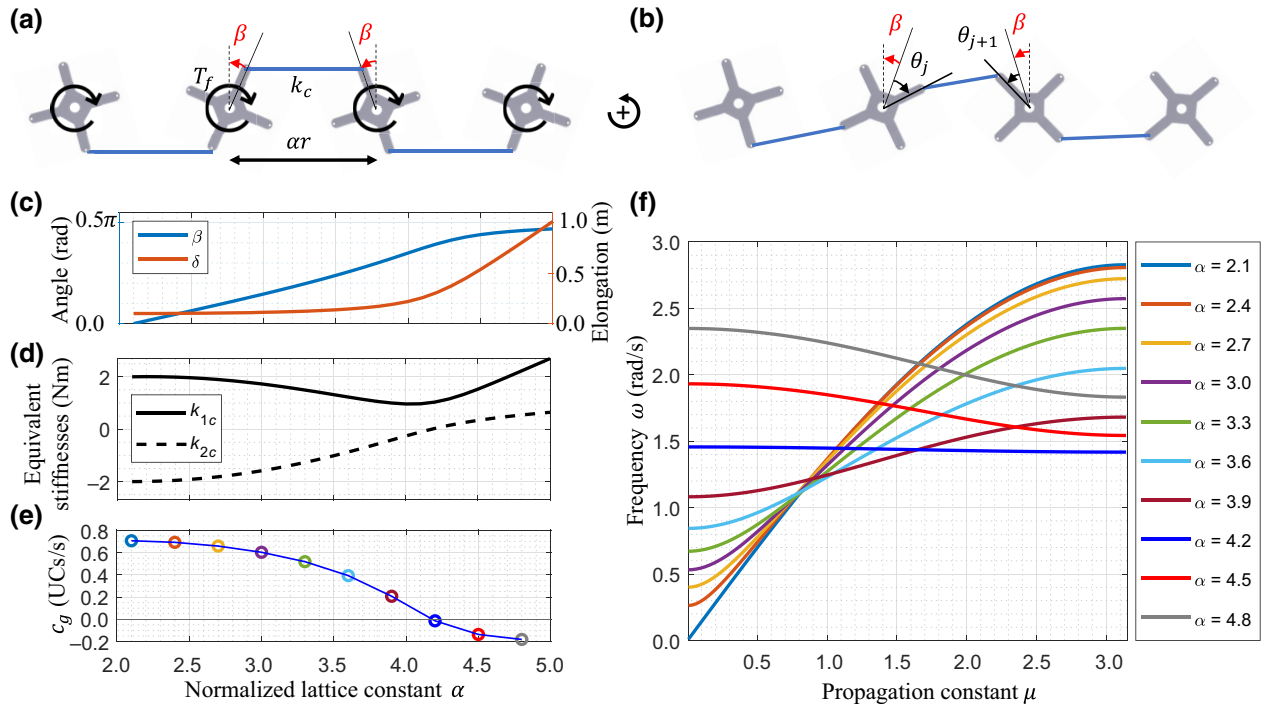


FIG. 2. (a) A schematic of a 1D CRL at its equilibrium position. The system parameters are illustrated. (b) A schematic of a CRL during motion. The compromising angle β and angular displacements θ_j and θ_{j+1} are illustrated. (c) The evolution of the compromising angle (blue curve) and spring elongation (red curve) as a function of the lattice constant. The blue and red curves correspond to the left and right vertical axes, respectively. (d) The evolution of the equivalent torsional stiffness with respect to the lattice constant. (e) The group velocity at $\mu = \pi/2$ for each dispersion curve presented in (f). (f) Dispersion curves at different normalized lattice constants.

III. TWO-DIMENSIONAL ADIABATIC LATTICE STRETCHING

In this section, we extend the 1D design concepts for SRLs and CRLs to two dimensions (2D) and investigate stretching-informed directivity changes and refraction steering.

A. Directivity engineering

In the 2D configuration illustrated in Fig. 3(a), we define a pair of offset angles, $\beta_{0,x}$ and $\beta_{0,y}$, characterizing the arms connecting the horizontal and vertical springs, respectively. The normalized lattice constants along the horizontal and vertical directions are defined as α_x and α_y , respectively. The governing equation of motion can be derived as

$$I\ddot{\theta}_{m,n} + \epsilon(2K_{1s,x}(t)\theta_{m,n} + K_{2s,x}(t)\theta_{m+1,n} + K_{2s,x}(t)\theta_{m-1,n+1} + 2K_{1s,y}(t)\theta_{m,n} + K_{2s,y}(t)\theta_{m,n-1} + K_{2s,y}(t)\theta_{m,n+1}) + O(\epsilon^2) = 0, \quad (13)$$

where (m, n) denotes the coordinates of the rotator of interest and subscripts “ x ” and “ y ” identify the parameters in the horizontal and vertical direction, respectively. In each direction, the inter-rotator interaction is identical to that of the 1D SRL and the equivalent torsional stiffnesses can be derived using the same formulas documented in Appendix B. Under adiabatic lattice deformation, we compute the dispersion relationship,

$$\omega = \sqrt{\frac{2K_{1s,x} + 2K_{2s,x} \cos \mu_x + 2K_{1s,y} + 2K_{2s,y} \cos \mu_y}{I}}, \quad (14)$$

where μ_x and μ_y are the propagation constants along the horizontal and vertical axes. The group velocities along both directions are derived accordingly:

$$c_{g,x} = \frac{\partial \omega}{\partial \mu_x} = -\frac{\sin(\mu_x)K_{2s,x}}{I\omega}, \quad (15)$$

$$c_{g,y} = \frac{\partial \omega}{\partial \mu_y} = -\frac{\sin(\mu_y)K_{2s,y}}{I\omega}. \quad (16)$$

In Figs. 3(b)–3(f), we present a numerical study of a 2D SRL to demonstrate the diverse directivity patterns induced by adiabatic dispersion morphing. The propagation patterns from a single source are simulated in MATLAB via direct numerical integration of the governing equation, Eq. (13), using the function ODE45.

The proposed 2D SRL example utilizes offset angles $\beta_{0,x} = \beta_{0,y} = 5\pi/18$ and initial (unstretched) lattice constants, $\alpha_x = \alpha_y = \alpha = 2.8$. The remaining system parameters correspond to those of the 1D SRL system, as given in Table I.

In Figs. 3(b)–3(d), we apply small adiabatic stretches ($\leq 5\%$) along the horizontal direction, while considering the same excitation frequency of 3.25 rad/s. We show that this subtle change effectively shifts the dispersion curve and generates distinct group-velocity contours. The simulated propagation patterns transition from circular to rectangular and eventually to angled beaming, verifying the group-velocity contours.

In Fig. 3(e), we stretch the lattice horizontally toward its critical lattice constant $\alpha_x^* = 1.27\alpha$ [recall Eq. (4)]. In the dispersion diagram, we observe a significant upshift of the pass band compared to Figs. 3(b)–3(d) but, more importantly, a plateau emerges from X to M (second-column subfigure), indicating the presence of a flat band in the horizontal direction. Accordingly, we consider an excitation frequency $\omega = 3.55$ rad/s in the pass band. The resultant group-velocity contour (third-column subfigure) contains only two points with zero horizontal components, which implies that the propagation of Bloch waves is strictly vertical. In fact, this flat band disables all the equivalent linear horizontal couplings in the 2D lattice ($K_{2s,x} = 0$) and the 2D lattice can be interpreted as segmented vertical stripes of monatomic chains; had higher-order terms been included in the Taylor expansion, nonlinear stiffness terms would appear and be nonzero, but their effect is negligible for the amplitudes considered. The numerical simulation confirms this phenomenon (fourth-column subfigure).

Symmetrically, a vertical stretch can induce similar directivity reconfiguration. We show in Fig. 3(f) that a vertical stretch approaching the critical lattice constant $\alpha_y^* = 1.27\alpha$ contributes to a strict horizontal propagation. As such, we demonstrate the vast potential of dispersion morphing for directivity engineering. The results in Figs. 3(e) and 3(f) suggest a promising stretching-informed bidirectional waveguide, which may find applications in multiplexing and/or demultiplexing [18].

B. Real-time refraction steering

Another exemplary effect that arises from dispersion morphing is the ability to change the refractive index. In Sec. II B, we have demonstrated that an adiabatic stretch in a CRL can alter the sign of the refractive index without excessively shifting the pass band. In this section, we use this property to engineer a real-time refraction-steering device.

We construct a 2D interface system with an SRL as the incident medium and a CRL as the receiving medium. The 2D SRL, as shown in Fig. 4(a), utilizes offset angles, $\beta_{0,x} = \beta_{0,y} = 0$, identical to the side-arm-connected lattice studied in Ref. [36]. The horizontal and vertical lattice constants are assumed equal to each other at all times and are represented by $\alpha(t)$. We employ the same rotator and spring parameters in Table I. This 2D SRL, by design, has a stretching-immune dispersion relationship, since its

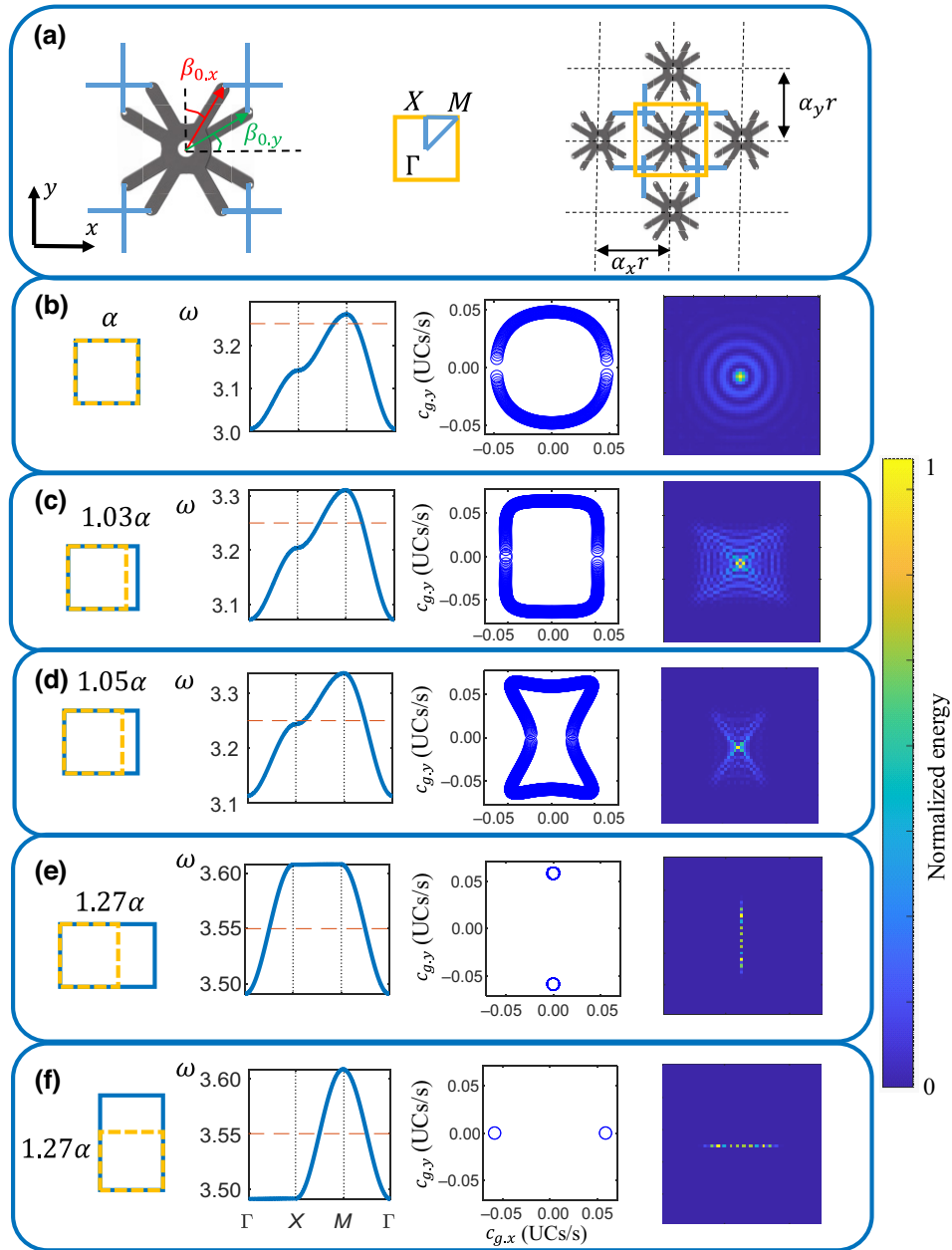


FIG. 3. Directivity patterns for an adiabatically stretched 2D SRL. (a) The 2D SRL unit-cell design and the Wigner-Seitz cell notation. (b)–(f) In each subfigure, from left to right, we show schematics of the lattice stretching, dispersion curve, group-velocity contour, and numerically simulated energy-propagation pattern. In the dispersion diagram, the red dashed line indicates the excitation frequency. The numerical simulation results illustrate the pixelated energy at each unit cell, normalized to be between 0 and 1. The physical dimensions of the deformed unit cells are not illustrated.

equivalent stiffnesses are not a function of $\alpha(t)$:

$$\begin{aligned} K_{1s,x} &= K_{1s,y} = 2k_s r^2, \\ K_{2s,x} &= K_{2s,y} = -2k_s r^2. \end{aligned} \quad (17)$$

In this way, its refractive index does not change with lattice stretching. The governing equation of motion of the incident medium is identical to Eq. (13) and the dispersion relationship follows Eq. (14).

In the receiving medium [Fig. 4(b)], we specify a 2D extension of a 1D CRL the refractive index of which changes with lattice stretching. We adopt the same rotator and spring parameters described in Table II and the same dimensionless lattice constant as the incident SRL, $\alpha(t)$. The external torque applied on each rotator, however, doubles the value used in the 1D configuration: $\Gamma_0^{2D} = 2\Gamma_0$. In addition, we consider a light grounding damping term ($D = 0.1 \text{ N m s}$) at each rotator to dissipate transient

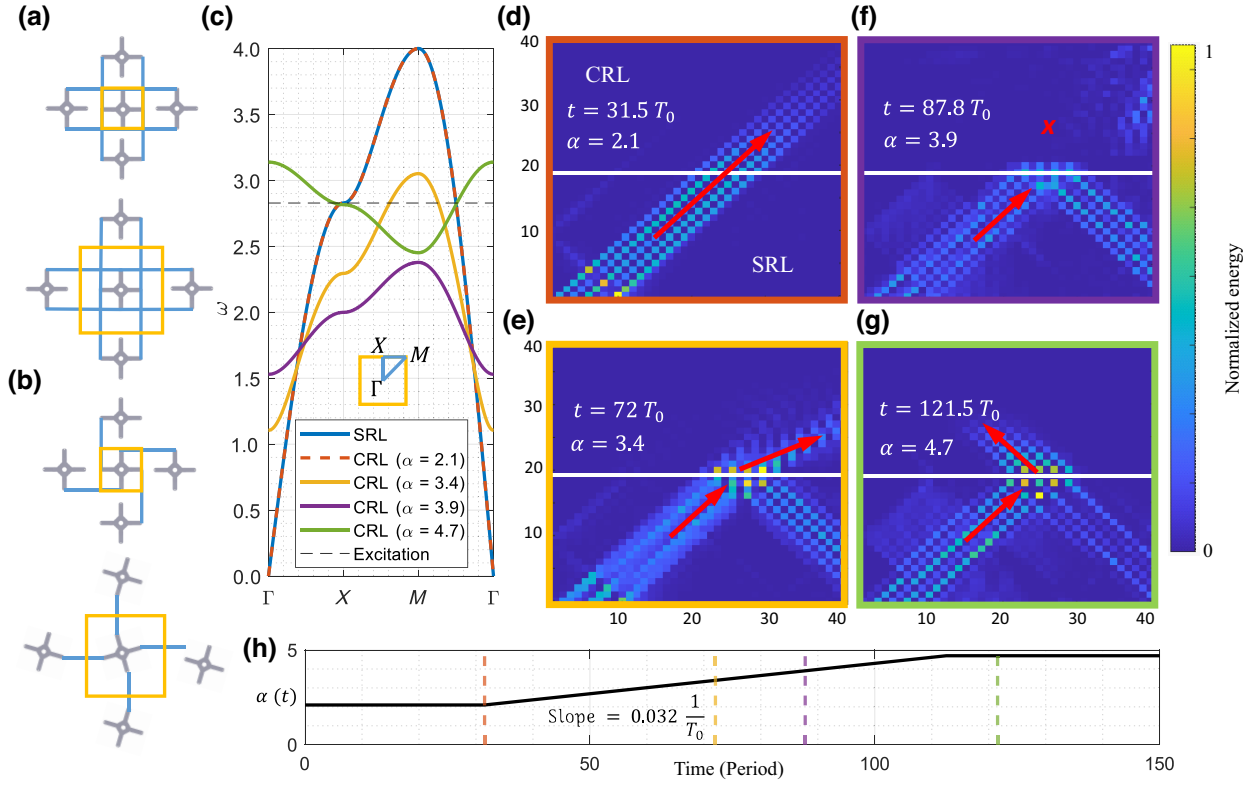


FIG. 4. An illustration of refraction steering on an SRL-CRL interface system. (a) The schematics of the incident SRL. The top and bottom configurations denote the initial state and the stretched state of the lattice. (b) The schematics of the receiving CRL. The top and bottom configurations denote the initial state and the stretched state of the lattice. (c) The band structure of the incident and receiving media. The black dashed line denotes the excitation frequency. (d)–(g) The numerical simulated energy-propagation pattern of the interface system under different lattice stretches. The pixelated energy distribution is normalized between 0 and 1. The white line represents the interface between two media and the red arrows the direction of propagation. The boundary color of each subplot matches the associated dispersion curve in (c). (h) The time history of the lattice constant under adiabatic stretching. The time is measured in terms of the wave period T_0 .

forms of behavior associated with loading. The governing equation can be gleaned from Eq. (10) as

$$I\ddot{\theta}_{m,n} + \epsilon(2K_{1c,x}\theta_{m,n} + K_{2c,x}\theta_{m,n-1} + K_{2c,x}\theta_{m,n+1} + 2K_{1c,y}\theta_{m,n} + K_{2c,y}\theta_{m-1,n} + K_{2c,y}\theta_{m+1,n}) + D\dot{\theta}_{m,n} + O(\epsilon^2) = 0. \quad (18)$$

The subscript (m, n) represents the horizontal and vertical indices of a rotator. We derive the dispersion relationship accordingly:

$$\omega = \sqrt{\frac{2K_{1c,x} + 2K_{2c,x} \cos \mu_x + 2K_{1c,y} + 2K_{2c,y} \cos \mu_y}{I}}. \quad (19)$$

Figure 4(c) depicts the dispersion curves of the SRL and CRL at a selection of lattice constants.

To investigate refraction steering, we layer the two lattices as shown in Fig. 4(d), and utilize a 45° incident wave at frequency $(\omega = 2\sqrt{2} \text{ rad/s})$. At the interface (vertical coordinate $n = n^*$), the two media are connected by

an array of linear couplings with stiffness identical to the vertical equivalent stiffness in the SRL: $K_t = K_{1s,y}$. In practice, these couplings can be realized by stacking one rotator on top of another in the third dimension such that they share the same rotation axis and then coupling them with a linear torsional spring. This method avoids the incompatibility of two types of rotator connections in each lattice. As such, we present the equations of motion for the boundary rotators in SRLs and CRLs, respectively,

SRL boundary rotators :

$$I\ddot{\theta}_{m,n^*-1} + \epsilon(2K_{1s,x}\theta_{m,n^*-1} + K_{2s,x}\theta_{m-1,n^*-1} + K_{2s,x}\theta_{m+1,n^*-1} + K_{1s,y}\theta_{m,n^*-1} + K_{2s,y}\theta_{m,n^*-2} + K_t(\theta_{m,n^*-1} - \theta_{m,n^*})) + O(\epsilon^2) = 0, \quad (20)$$

CRL boundary rotators :

$$I\ddot{\theta}_{m,n^*} + \epsilon(2K_{1c,x}\theta_{m,n^*} + K_{2c,x}\theta_{m-1,n^*} + K_{2c,x}\theta_{m+1,n^*} + K_{1c,y}\theta_{m,n^*} + K_{2c,y}\theta_{m,n^*+1} + K_t(\theta_{m,n^*} - \theta_{m,n^*-1})) + D\dot{\theta}_{m,n} + O(\epsilon^2) = 0. \quad (21)$$

During the wave propagation, we slowly stretch the lattice system (both SRL and CRL) horizontally and vertically, such that the lattice constants in both directions undergo the same process of increasing, as illustrated in Fig. 4(h). We use the wave period, $T_0 = 2\pi/\omega = 2.22s$, as the measure of time and document the increasing rate of the lattice constants as 0.032 units per period, significantly slower than the wave dynamics. Hence, we consider the stretching process to be adiabatic. During the deformation, the SRL unit cell admits the same shape with elongated springs in both directions, shown in the bottom configuration of Fig. 4(a). The CRL unit cell, however, undergoes an equilibrium shift, which alters the rotational geometry, as depicted in the bottom of Fig. 4(b). In the dispersion diagram [Fig. 4(c)], we observe a similar phenomenon as illustrated in Fig. 2(e), where the dispersion curve first shifts down, with the pass band narrowed, and then rises up as an optical branch with a negative group velocity in each lattice direction. Since the dispersion curve of the incident medium remains an acoustic type in this process, the lattice stretching refracts the transmission at the interface from positive to negative.

We illustrate refraction steering in numerical simulations documented in Figs. 4(d)–4(g). At the initial configuration ($\alpha = 2.1$), the dispersion curves of the incident and receiving media are overlaid on each other, as shown in Fig. 4(c). With the impedance matching, we observe a full positive transmission in Fig. 4(d). As the lattice stretches in real time, this refraction starts to bend away from the interface normal, as shown in Fig. 4(e). At $\alpha = 3.9$, the pass band of the receiving lattice shifts down and no longer contains the excitation frequency, thus forbidding any transmission in Fig. 4(f). Finally, Fig. 4(g) depicts a negative refraction at $\alpha = 4.7$, when the CRL pass band rises and contains the excitation frequency again. Therefore, we demonstrate a real-time refraction-steering device utilizing adiabatic dispersion morphing in the 2D CRL.

IV. NONADIABATIC LATTICE STRETCHING

In this section, we apply nonadiabatic (dynamic) lattice stretching to demonstrate the propagation-delay and parametric amplification phenomena in SRLs.

A. On-demand propagation delay

We first propose a stretching-controlled signal-delay device utilizing the nonadiabatic dispersion morphing in a 2D SRL. We consider a 2D SRL with offset angles $\beta_{0,x} = \beta_{0,y} = \pi/4$ and refer to Table I for the remaining parameters. The equation of motion of this lattice takes a form identical to Eq. (13).

We excite the system with a source array placed at the bottom-left corner (S) of the 2D lattice and distribute two receivers at the top-right corner (R) and at the center of the lattice (c), respectively, as illustrated in Fig. 5(a). The

source array emits a 45° finite signal at frequency $\omega_A = 3.15$ rad/s toward R.

During the propagation, we apply nonadiabatic stretches of equal magnitude ($\alpha(t) = \alpha_x(t) = \alpha_y(t)$) along both the horizontal and the vertical directions, as shown in Fig. 5(b). Different from the slow stretching described in Fig. 4(h), these nonadiabatic stretches result in rapid changes of the lattice constant. To facilitate analytical exploration, we model the rapid change as instantaneous increasing or decreasing, as illustrated in Fig. 5(c). As depicted, the lattice constant rises from 2.8 to 5 at moment $t = t_1$ and drops back at $t = t_2$. We label the $\alpha = 2.8$ configuration as state *A* and the $\alpha = 5$ configuration as state *B*. Within each state, the dispersion relationship, which we present in Fig. 5(d), takes the form of Eq. (14). Since the state transition at t_1 and t_2 is nonadiabatic, we employ a temporal-interface model to formulate the wave dynamics at these transitioning moments.

We analyze the temporal interface at $t = t_1$ as an example. Right before the temporal interface ($t \rightarrow t_1^-$), we assume a Bloch-wave solution in the lattice domain,

$$\theta_{m,n}^-(t, \mathbf{r}) = A e^{i(\omega_A t - \boldsymbol{\mu} \cdot \mathbf{r})}, \quad (22)$$

where $\boldsymbol{\mu} = \mu_x \mathbf{x} + \mu_y \mathbf{y}$ and $\mathbf{r} = m\mathbf{x} + n\mathbf{y}$ denote the dimensionless wave vector (i.e., the 2D propagation constant) and the dimensionless position vector, respectively, and \mathbf{x} and \mathbf{y} denote unit vectors in the horizontal and vertical directions. Right after the first temporal interface ($t \rightarrow t_1^+$), the wave solution can be assumed to be a combination of infinitely many Bloch waves, the spatial and temporal frequencies of which obey the dispersion relationship at state *B*,

$$\theta_{m,n}^+(t, \mathbf{r}) = \sum_s A_s e^{i(\omega_s t - \boldsymbol{\mu}_s \cdot \mathbf{r})}, \quad (23)$$

where A_s , ω_s , and $\boldsymbol{\mu}_s$ are the amplitude, frequency and dimensionless wave vector of the *s*th Bloch-wave solution at state *B*. At $t = t_1$, the continuity in displacement and velocity yields [38],

$$\theta_{m,n}^-(t = t_1^-, \mathbf{r}) = \theta_{m,n}^+(t = t_1^+, \mathbf{r}), \quad (24)$$

$$\frac{\partial \theta_{m,n}^-}{\partial t} \Big|_{t=t_1^-} = \frac{\partial \theta_{m,n}^+}{\partial t} \Big|_{t=t_1^+}. \quad (25)$$

Substitution of Eqs. (22) and (23) into Eqs. (24) and (25) yields $\boldsymbol{\mu}_s = \boldsymbol{\mu}$ and $\omega_s = \pm \omega_B(\boldsymbol{\mu})$, where $\omega_B(\boldsymbol{\mu})$ is the frequency at $\boldsymbol{\mu}$ at state *B*. This result suggests a preservation on propagation constant but a change in frequency across the temporal interface [38] as highlighted by the dashed lines in Fig. 5(d). This frequency jump is numerically verified in the response at receiver C, shown in Figs. 5(e) and 5(f).

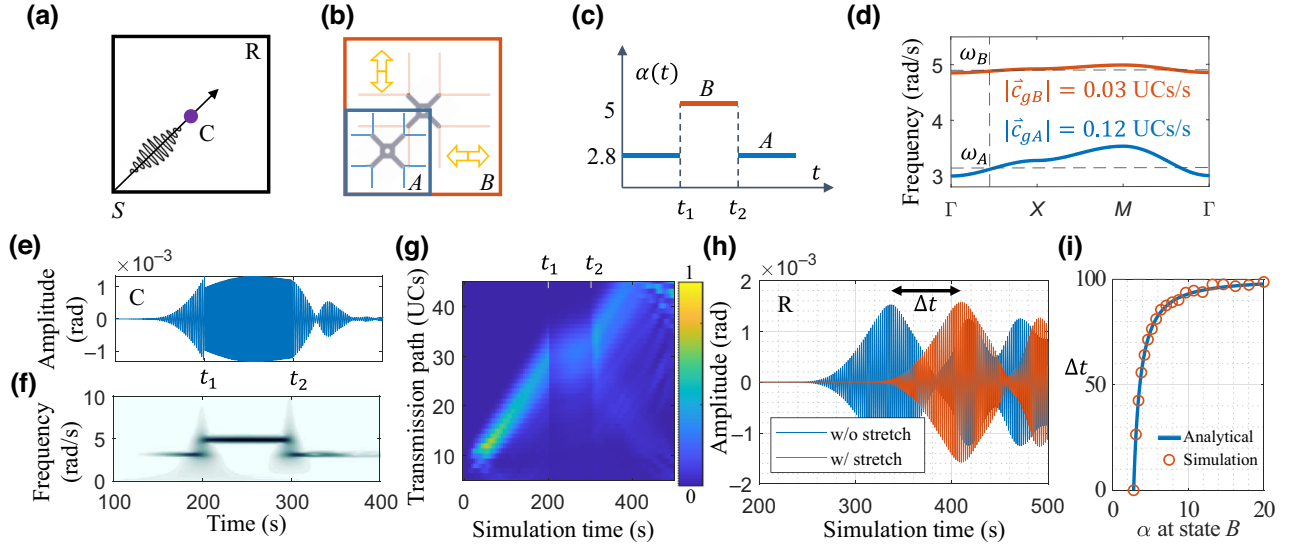


FIG. 5. (a) A schematic of the SRL model, with the propagation direction, source S , receiver R , and center C marked. (b) The lattice configuration at states A and B . (c) The lattice constant as a function of time. For numerical evaluation, $t_1 = 200$ s and $t_2 = 300$ s. (d) The band structure at two states, A and B . The horizontal dashed lines indicate the wave frequency in each state. The vertical dashed line represents the wave vector in both states. Group velocities at both configurations are evaluated. (e) The time response at C . (f) The wavelet response at C . (g) The pixelated energy distribution along the transmission path [indicated in (a)] as a function of time. (h) The time responses of the signal received at R . The receiving signal from a lattice without stretching is provided as a reference. (i) The signal delay as a function of the stretching at state B .

Accordingly, Eq. (23) is simplified and only includes two waves sharing the same wave vector but propagating in opposite directions:

$$\theta_{m,n}^+ = A_+ e^{i(\omega_B t - \mu \cdot \mathbf{r})} + A_- e^{i(-\omega_B t - \mu \cdot \mathbf{r})}. \quad (26)$$

The linear system described by Eqs. (24) and (25) also yields the corresponding amplitude coefficients A_+ and A_- :

$$A_+ = \frac{\omega_B + \omega_A}{2\omega_B} A, \quad A_- = \frac{\omega_B - \omega_A}{2\omega_B} A. \quad (27)$$

Since $\omega_B > \omega_A > 0$, as illustrated in Fig. 5(d), the forward wave carries larger energy ($A_+ > A_-$). Typically, after each temporal interface, the number of waves doubles. In a single rectangular function that includes two state transitions, as depicted in Fig. 5(c), the incident wave splits into four (two forward and two backward). The two forward waves, spaced slightly apart due to the propagation during state B , exhibit different amplitudes. For time-delay considerations, we confine our interest to the first forward wave that arrives at receiver R . The amplitude of the considered forward wave is given by

$$A_{++} = \frac{\omega_A + \omega_B}{2\omega_A} A_+ = \frac{(\omega_A + \omega_B)^2}{4\omega_A \omega_B} A. \quad (28)$$

Numerically evaluating this expression yields the amplitude $A_{++} = 1.05A$, matching qualitatively the numerical observation of $1.03A$ measured from the simulation.

Some discrepancy arises from (i) the numerical simulation employing a center-frequency wave packet composed of multiple frequencies, each having their own amplification [unlike the single plane wave considered in Eq. (28)], and (ii) the difficulty associated with separating the two forward waves from each other.

In Fig. 5(g), we depict the energy flow along the transmission path. The slowing effect during state B contributes to a time delay in the propagation when compared to the reference signal without the rectangular modulation on the lattice constant, as depicted in Fig. 5(h). We compute the time delay between two signals as

$$\Delta t = \frac{c_{gA} - c_{gB}}{c_{gA}} (t_2 - t_1), \quad (29)$$

where c_{gA} and c_{gB} represent the group velocity of the wave vector at states A and B , respectively. We note that this time delay is proportional to the difference of the two group velocities and the duration of state B . By altering either factor, one may control the time delay of a propagating signal. Evaluating this quantity with the system parameters yields a delay of $\Delta t = 73$ s, matching the observed delay $\Delta t = 71.52$ s measured in Fig. 5(h). In fact, larger stretching at state B leads to a higher and narrower pass band and thus a longer time delay. At exceptionally large stretching, the group velocity approaches zero, $c_{gB} \rightarrow 0$, freezing the signal in space during state B . Thus the delay approaches

the duration of state B ,

$$\Delta t \rightarrow t_2 - t_1. \quad (30)$$

We illustrate and numerically validate this trend in Fig. 5(i), for a wide range of stretching. This ability to reconfigure delay suggests straightforward application to delay-line engineering [43] and logic devices [18,44].

B. Parametric amplification

In addition to the instantaneous lattice stretching investigated above, we also examine the effects of a harmonic modulation on dispersion morphing. We note that this type of periodic deformation is ubiquitous in physical systems: e.g., breathing mechanisms and thermal fatigue. For simplicity, we consider a 1D SRL with $\beta_0 = \pi/2$, as depicted in Fig. 6(a). The harmonic modulation acts synchronously on all lattice spacing such that $\alpha(t) = \alpha_0(1 + \epsilon\lambda_m \cos(\omega_m t))$, where $\epsilon\lambda_m$ and ω_m are the modulation amplitude and frequency, respectively. The reference amplitude α_0 is set to be 2.8 and the modulation amplitude is denoted as being small ($\epsilon\lambda_m \ll 1$). The small parameter ϵ allows us to Taylor expand the equivalent stiffness expressions and quantify the stretching-induced time dependence in a hierarchical order,

$$\begin{aligned} K_{1s}(t) &= 2k_s r^2 \left(1 - \frac{L_s}{r} \frac{1}{\alpha(t) - 2} \right) (\alpha(t) - 1) \\ &= 2k_s r^2 \left(1 - \frac{L_s}{r} \frac{1}{\alpha_0(1 + \epsilon\lambda_m \cos(\omega_m t)) - 2} \right) \\ &\quad \times (\alpha_0(1 + \epsilon\lambda_m \cos(\omega_m t)) - 1) \\ &= \widehat{k}_1 (1 + \epsilon X \cos(\omega_m t)) + O(\epsilon^2), \end{aligned} \quad (31)$$

$$\begin{aligned} K_{2s}(t) &= 2k_s r^2 \left(1 - \frac{L_s}{r} \frac{1}{\alpha(t) - 2} \right) \\ &= 2k_s r^2 \left(1 - \frac{L_s}{r} \frac{1}{\alpha_0(1 + \lambda_m \cos(\omega_m t)) - 2} \right) \\ &= \widehat{k}_2 (1 + \epsilon Y \cos(\omega_m t)) + O(\epsilon^2), \end{aligned} \quad (32)$$

where

$$\widehat{k}_1 = 2k_s r^2 \left(1 - \frac{L_s}{r} \frac{1}{\alpha_0 - 2} \right) (\alpha_0 - 1), \quad (33)$$

$$X = \frac{\alpha_0 \lambda_m (r\alpha_0^2 - 4r\alpha_0 + 4r + L_s)}{(\alpha_0 - 2)(r\alpha_0 - L_s - 2r)(\alpha_0 - 1)}, \quad (34)$$

$$\widehat{k}_2 = 2k_s r^2 \left(1 - \frac{L_s}{r} \frac{1}{\alpha_0 - 2} \right), \quad (35)$$

$$Y = \frac{L_s \alpha_0 \lambda_m}{(\alpha_0 - 2)(r(\alpha_0 - 2) - L_s)}. \quad (36)$$

At the two leading orders, the periodic stretching results in equivalent harmonic stiffnesses. The higher-order terms (containing higher harmonics of the modulation frequency) have negligible magnitude at small modulation amplitude and are thus omitted in the following analysis. We now formulate the solution to Eq. (1) with harmonic stiffness in Floquet form [21,45],

$$\theta_j = C \sum_{n=-\infty}^{n=+\infty} (\widehat{p}_n e^{in\omega_m t}) e^{i(\omega t - \mu j)}, \quad (37)$$

where C denotes the wave amplitude and \widehat{p}_n denotes the n th Fourier coefficient. Substituting Eqs. (31)–(37) into Eq. (1) and collecting harmonic terms at $n\omega_m t$ yields

$$\begin{aligned} I \sum_{n=-\infty}^{n=+\infty} (\omega + n\omega_m)^2 \widehat{p}_n e^{in\omega_m t} \\ = U \sum_{n=-\infty}^{n=+\infty} \widehat{p}_n e^{in\omega_m t} + V \sum_{n=-\infty}^{n=+\infty} \widehat{p}_n e^{i(n+1)\omega_m t} \\ + V \sum_{n=-\infty}^{n=+\infty} \widehat{p}_n e^{i(n-1)\omega_m t}, \end{aligned} \quad (38)$$

where $U = 2\widehat{k}_1 + 2\widehat{k}_2 \cos(\mu)$ and $V = \epsilon\widehat{k}_1 X + \epsilon\widehat{k}_2 Y \cos(\mu)$. To remove the time dependence in Eq. (38), we compute the inner product with $e^{in\omega_m t}$, yielding a quadratic eigenvalue problem for ω (with the associated Hill determinant [46]),

$$I(\omega^2 + 2n\omega_m \omega + n^2 \omega_m^2) \widehat{p}_n = U \widehat{p}_n + V(\widehat{p}_{n-1} + \widehat{p}_{n+1}), \quad (39)$$

where $n \in (-\infty, \infty)$ is an integer. The solution to this equation describes a frequency-periodic dispersion spectrum [21]. To facilitate numerical evaluation, we truncate the series, $n \in \{-1, 0, 1\}$ and obtain a 3×3 matrix the eigenvalues of which reveal the dispersion characteristics in our time-modulated lattice. We justify the truncated selection of n in Appendix C.

In Fig. 6(b), we compute dispersion relationships for four pairs of modulation frequencies and amplitudes. Blue denotes real frequency components while red denotes imaginary components. Unlike time-invariant systems, the time modulation generates a series of dispersion curves shifted from the static set. When the real components of frequency meet, they morph into a sectional flat band where the eigenfrequencies become complex. These complex eigenfrequencies appear as pairs of complex conjugates and lead to exponential growth of the wave amplitude

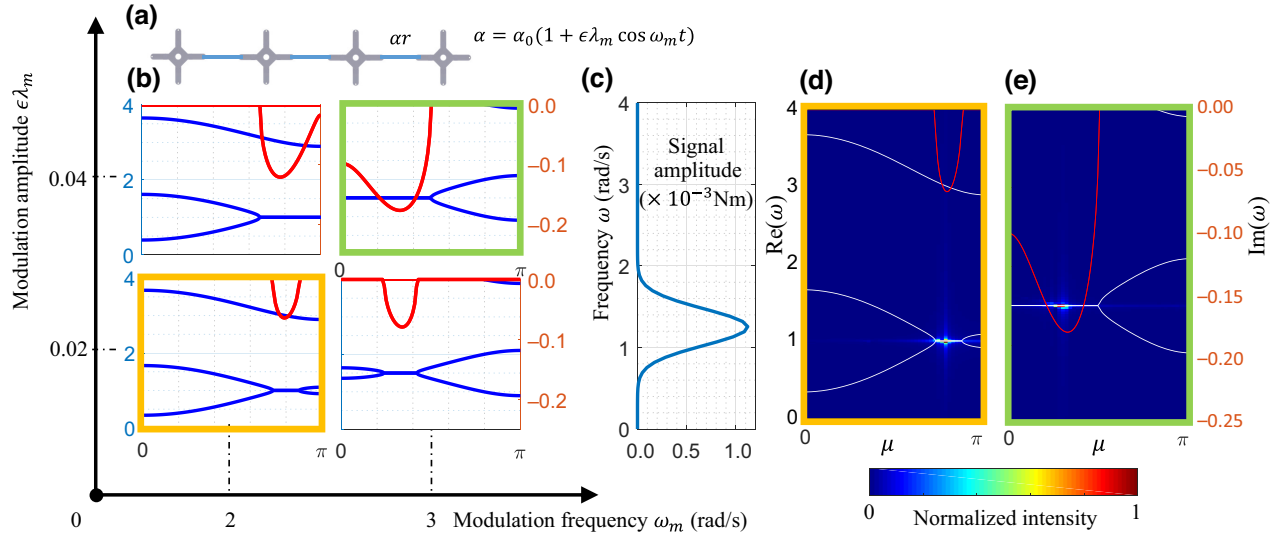


FIG. 6. (a) A schematic of the harmonic time-modulated 1D SRL. (b) Dispersion diagrams at various modulation amplitudes and frequencies. The blue curves represent the real component of the eigenfrequency and correspond to the vertical axis on the left of each subplot. The red curves denote the imaginary component and correspond to the vertical axis on the right of each subplot. The horizontal axis denotes the propagation constant in the first Brillouin zone from 0 to π . (c) The excitation signal used in numerical simulations. (d),(e) 2D fast-Fourier-transform (FFT) results ($200 \leq t \leq 400$ s, $1 \leq j \leq 100$) for the 1D lattice subject to the signal depicted in (c): (d) real; (e) imaginary. The border colors (orange and green) correspond to the modulation amplitudes and frequencies with the same border colors as in (b). The associated dispersion curves are superposed on the FFT results in white [$\text{Re}(\omega)$] and red [$\text{Im}(\omega)$]. The left vertical axis corresponds to the real component of the frequency and the right one to the imaginary component.

in time, known as parametric amplification [21,47]. The dominant growth emerges at a pair of frequency and propagation constants (ω^* , μ^*) with maximal imaginary magnitude $|\text{Im}(\omega^*)|$. We show in Fig. 6(b) that the location of this critical pair can be reconfigured by adjusting the modulation frequency and amplitude. Specifically, the modulation frequency regulates the frequency location of the flat band $\omega^* = \omega_m/2$ —similar to parametric resonance, where the excitation frequency and a natural frequency are related by a factor of 2 [48]—and the modulation amplitude determines the length of the flat band and the growth rate (i.e., the magnitude of the imaginary frequency). We note that including more terms ($n = \pm 2, \pm 3, \dots$) in the series [Eq. (39)] generates larger matrices and more dispersion branches at higher frequencies. These dispersion branches are not in the excitation-frequency range in which we are interested. We provide more discussion in Appendix C.

Using the multifrequency signal shown in Fig. 6(c), we apply a finite torque signal ($y(t)$) at a boundary mass of the 1D SRL with a frequency content centered around $\omega = 1.25$ rad/s,

$$y(t) = 0.01e^{-0.025(t-20)^2} \cos(\omega t), \quad (40)$$

and simulate its propagation in the time-modulated lattice using direct numerical integration. To avoid unbounded growth, we introduce grounded viscous damping $D = 0.08$ N m s at each rotator. In Figs. 6(d) and 6(e), we conduct a 2D fast Fourier transform (FFT) to analyze the

dominant wave form in the lattice associated with two sets of modulation parameters, highlighted in orange and green borders in Fig. 6(b). In each subfigure, we recognize the critical frequency-propagation pair on the flat band where the imaginary component of the eigenfrequency is maximized, confirming the theory.

V. CONCLUDING REMARKS

Using symmetric and chiral rotator systems, we have explored dispersion morphing under adiabatic and nonadiabatic stretching. Under axial-lattice stretching, these lattices possess infinitely many stable configurations, allowing a high degree of reconfigurability for enabling flexible adaptations. Informed by adiabatic dispersion relationships, we have demonstrated bidirectional waveguiding and real-time refraction steering under static and quasistatic stretching. For nonadiabatic stretching, we have employed a temporal interface model and a Floquet-based Fourier expansion to analyze wave propagation under step and harmonic stretching. We have demonstrated on-demand propagation delay and, in extreme cases, propagation freezing. For small harmonic stretching, we have analytically and numerically demonstrated parametric amplification. Follow-on work from this study could include investigation of spatial-temporal modulation of rotator systems [35,36] and experimental demonstrations, which can be carried out in a straightforward manner similar to experiments detailed in Ref. [36].

ACKNOWLEDGMENTS

We would like to thank the National Science Foundation for support of this research under Civil, Mechanical, and Manufacturing Innovation (CMMI) Grant No. 1929849. L.F. would like to thank Sai Kuchibhatla and Dr. Yiwei Xia for insightful discussions about parametric amplification.

APPENDIX A: AN EXPERIMENTAL DESIGN FOR THE ROTATOR LATTICES

In this appendix, we propose an experimental design for a stretchable rotator lattice, which aims to enhance the visualization of the lattice structure and facilitate future experimental validation. Figure 7 illustrates a parallelogram-based mechanism built from T-slotted framing rails and pivots. The lengths of two edges of the parallelogram are fixed and denoted as s_1 and s_2 . An array of additional rails are uniformly distributed inside the parallelogram, enabling the construction of a 1D rotator lattice along one diagonal axis (the blue dashed line). Figure 7 depicts five rotators as an illustration, while the introduction of more rails inside the parallelogram structure

allows for the inclusion of more rotators. This mechanism allows prescribed rotator-lattice stretching using morphing of the parallelogram geometry. For example, one may fix the top-left corner of the parallelogram and prescribe the motion of the bottom-right corner. The lengths of both diagonals change during morphing and the lattice constant changes accordingly. We assume that the rigidity of the parallelogram structure is much higher than the inter-rotator coupling and thus the spacing between rotators can change uniformly and simultaneously. Further, this parallelogram structure has the potential to accommodate 2D rotator lattices as well, which we plan to explore in future investigations.

APPENDIX B: EQUIVALENT TORSIONAL STIFFNESS

In this appendix, we present the explicit forms for the equivalent torsional linear stiffnesses $K_{1s}(t)$ and $K_{2s}(t)$ in an SRL and $K_{1c}(t)$ and $K_{2c}(t)$ in a CRL. The SRL linear stiffnesses take the form

$$K_{1s}(t) = \frac{2k_s r^2 ((2 \cos^2 \beta_0 + \alpha \sin \beta_0 - 1) G^{\frac{3}{2}} - \frac{L_s}{r} (-4 \cos^4 \beta_0 + (5\alpha^2 - 8\alpha \sin \beta_0 + 8) \cos^2 \beta_0 + \alpha(\alpha^2 + 8) \sin \beta_0 - 5\alpha^2 - 4))}{G^{\frac{3}{2}}}, \quad (\text{B1})$$

$$K_{2s}(t) = \frac{2k_s r^2 \left((-2 \cos^2 \beta_0 + 1) G^{\frac{3}{2}} - \frac{L_s}{r} (4 \cos^4 \beta_0 + (4\alpha \sin \beta_0 - \alpha^2 - 8) \cos^2 \beta_0 - 4 \sin \beta_0 \alpha + \alpha^2 + 4) \right)}{G^{\frac{3}{2}}}, \quad (\text{B2})$$

$$G = \alpha^2 - 4\alpha \sin \beta_0 - 4 \cos^2 \beta_0 + 4, \quad (\text{B3})$$

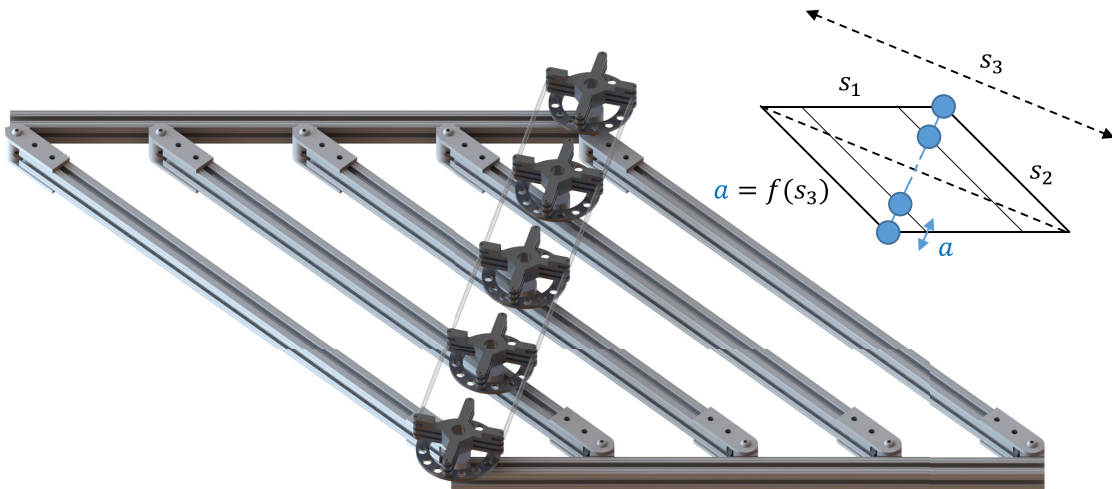


FIG. 7. The conceptual design of a 1D rotator lattice incorporating five rotators. The schematic at the top right describes a parallelogram-based mechanism, where the lattice constant a can be reconfigured via changes in the s_3 diagonal length.

where the time dependence on the right-hand side has been suppressed for the sake of brevity. In the CRL, the equivalent torsional stiffnesses, K_{1c} and K_{2c} , are equal to

$$K_{1c}(t) = \frac{k_c r^2 ((2 \cos^2 \beta + \alpha \sin \beta - 1) G^{\frac{3}{2}} - \frac{L_c}{r} (-4 \cos^4 \beta + (5\alpha^2 - 8\alpha \sin \beta + 8) \cos^2 \beta + \alpha(\alpha^2 + 8) \sin \beta - 5\alpha^2 - 4))}{G^{\frac{3}{2}}}, \quad (\text{B4})$$

$$K_{2c}(t) = \frac{k_c r^2 ((-2 \cos^2 \beta + 1) G^{\frac{3}{2}} - \frac{L_c}{r} (4 \cos^4 \beta + (4\alpha \sin \beta - \alpha^2 - 8) \cos^2 \beta - 4 \sin \beta \alpha + \alpha^2 + 4))}{G^{\frac{3}{2}}}, \quad (\text{B5})$$

$$G = \alpha^2 - 4\alpha \sin \beta - 4 \cos^2 \beta + 4. \quad (\text{B6})$$

APPENDIX C: HIGHER TRUNCATION NUMBER N AND FREQUENCY-PERIODIC DISPERSION SPECTRUM

In this appendix, we describe the frequency-periodic dispersion spectrum introduced in Eq. (39), with a higher truncation number $N = \max(n)$. We consider a modulation frequency $\omega_m = 2$ rad/s and amplitude $\epsilon \lambda_m = 0.02$. Figures 8(a)–8(c) illustrate the band structure computed using Eq. (39) for $N = 1, 2$, and 5. Consistent with the discussion in Sec. IV B, the dispersion merging and the resultant flat bands occur at $\omega^* = 2|n| - 1/2\omega_m$. Typically, a

higher truncation number N resolves dispersion branches at higher frequencies, which maintains a periodic pattern in the frequency. Since the signal considered in Fig. 6(c) is well below the second flat band, our primary interest is the shape of the first dispersion branch. Figures 8(d) and 8(e) illustrate a detailed view of the first branch computed using different values of N , where we observe nearly identical results (real and imaginary). Thus, we conclude that a truncation number $N = 1$ is sufficient to capture the flat-band amplification effect for the study in Sec. IV B.

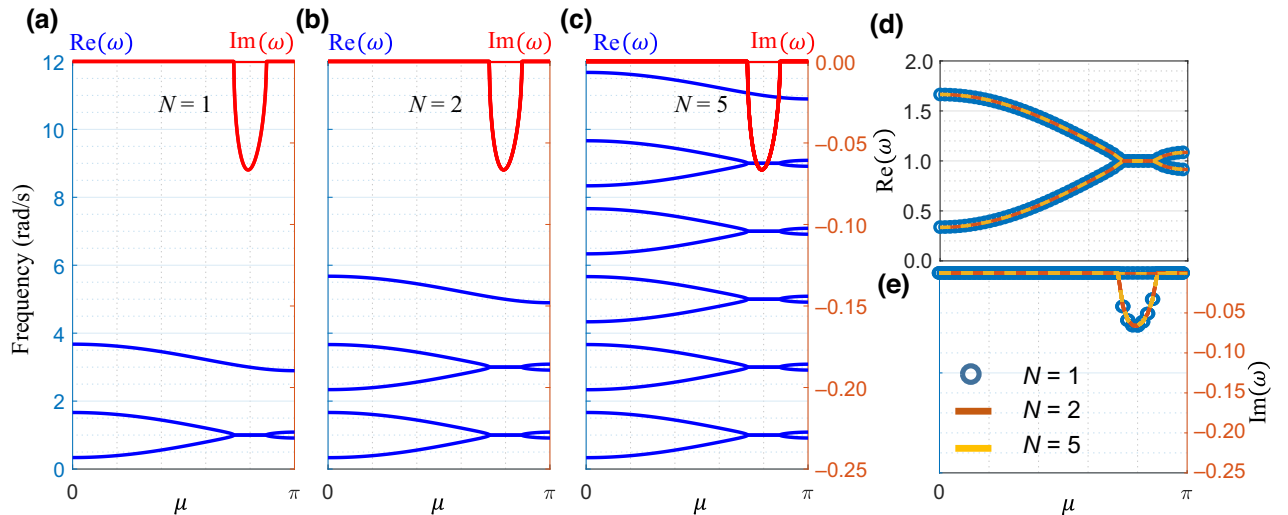


FIG. 8. (a)–(c) The frequency-dependent dispersive spectrum truncated at (a) $N = 1$, (b) $N = 2$, and (c) $N = 5$, respectively. The horizontal axis of each figure is the propagation constant μ . The blue curves represent the real component of the eigenfrequency and correspond to the left vertical axis; the red curves represent the imaginary component of the eigenfrequency and correspond to the right vertical axis. (d) A comparison of the first dispersion branches (real frequency) obtained using $N = 1$, $N = 2$, and $N = 5$. (e) A comparison of the first dispersion branches (imaginary frequency).

- [1] K. Bertoldi, V. Vitelli, J. Christensen, and M. Van Hecke, Flexible mechanical metamaterials, *Nat. Rev. Mater.* **2**, 1 (2017).
- [2] J. U. Surjadi, L. Gao, H. Du, X. Li, X. Xiong, N. X. Fang, and Y. Lu, Mechanical metamaterials and their engineering applications, *Adv. Eng. Mater.* **21**, 1800864 (2019).
- [3] R. Zhu, X. Liu, G. Hu, C. Sun, and G. Huang, Negative refraction of elastic waves at the deep-subwavelength scale in a single-phase metamaterial, *Nat. Commun.* **5**, 5510 (2014).
- [4] X.-N. Liu, G.-K. Hu, G.-L. Huang, and C.-T. Sun, An elastic metamaterial with simultaneously negative mass density and bulk modulus, *Appl. Phys. Lett.* **98**, 251907 (2011).
- [5] Y. Wu, Y. Lai, and Z.-Q. Zhang, Elastic Metamaterials with Simultaneously Negative Effective Shear Modulus and Mass Density, *Phys. Rev. Lett.* **107**, 105506 (2011).
- [6] Y. Chen, J. Hu, and G. Huang, A design of active elastic metamaterials for control of flexural waves using the transformation method, *J. Intell. Mater. Syst. Struct.* **27**, 1337 (2016).
- [7] P. Celli and S. Gonella, Tunable directivity in metamaterials with reconfigurable cell symmetry, *Appl. Phys. Lett.* **106**, 091905 (2015).
- [8] D. Beli, M. I. N. Rosa, C. De Marqui Jr, and M. Ruzzene, Wave beaming and diffraction in quasicrystalline elastic metamaterial plates, *Phys. Rev. Res.* **4**, 043030 (2022).
- [9] S.-H. Kim and M. P. Das, Seismic waveguide of metamaterials, *Mod. Phys. Lett. B* **26**, 1250105 (2012).
- [10] C. Sugino, S. Leadenham, M. Ruzzene, and A. Erturk, On the mechanism of bandgap formation in locally resonant finite elastic metamaterials, *J. Appl. Phys.* **120**, 134501 (2016).
- [11] E. Miranda Jr, E. Nobrega, A. Ferreira, and J. Dos Santos, Flexural wave band gaps in a multi-resonator elastic metamaterial plate using Kirchhoff-Love theory, *Mech. Syst. Signal Process.* **116**, 480 (2019).
- [12] M. H. Bae and J. H. Oh, Amplitude-induced bandgap: New type of bandgap for nonlinear elastic metamaterials, *J. Mech. Phys. Solids* **139**, 103930 (2020).
- [13] A. Srivastava, Elastic metamaterials and dynamic homogenization: A review, *Int. J. Smart Nano Mater.* **6**, 41 (2015).
- [14] L. Xin, Y. Siyuan, L. Harry, L. Minghui, and C. Yanfeng, Topological mechanical metamaterials: A brief review, *Current Opinion Solid State Mater. Sci.* **24**, 100853 (2020).
- [15] H. Huang, J. Chen, and S. Huo, Recent advances in topological elastic metamaterials, *J. Phys.: Condens. Matter* **33**, 503002 (2021).
- [16] J. Ji, Q. Luo, and K. Ye, Vibration control based metamaterials and origami structures: A state-of-the-art review, *Mech. Syst. Signal Process.* **161**, 107945 (2021).
- [17] S. Dalela, P. Balaji, and D. Jena, A review on application of mechanical metamaterials for vibration control, *Mech. Adv. Mater. Struct.* **29**, 3237 (2022).
- [18] A. Darabi, E. Kliewer, and M. J. Leamy, Reconfigurable acoustic multiplexer/demultiplexer using time division, *Appl. Phys. Lett.* **119**, 113501 (2021).
- [19] Z. Ren, L. Ji, R. Tao, M. Chen, Z. Wan, Z. Zhao, and D. Fang, SMP-based multi-stable mechanical metamaterials: From bandgap tuning to wave logic gates, *Extreme Mech. Lett.* **42**, 101077 (2021).
- [20] U. Waheed, C. Myant, and S. Dobson, Boolean and/or mechanical logic using multi-plane mechanical metamaterials, *Extreme Mech. Lett.* **40**, 100865 (2020).
- [21] G. Trainiti, Y. Xia, J. Marconi, G. Cazzulani, A. Erturk, and M. Ruzzene, Time-Periodic Stiffness Modulation in Elastic Metamaterials for Selective Wave Filtering: Theory and Experiment, *Phys. Rev. Lett.* **122**, 124301 (2019).
- [22] Y. Chen, X. Li, H. Nassar, A. N. Norris, C. Daraio, and G. Huang, Nonreciprocal Wave Propagation in a Continuum-Based Metamaterial with Space-Time Modulated Resonators, *Phys. Rev. Appl.* **11**, 064052 (2019).
- [23] F. Casadei, T. Delpero, A. Bergamini, P. Ermanni, and M. Ruzzene, Piezoelectric resonator arrays for tunable acoustic waveguides and metamaterials, *J. Appl. Phys.* **112**, 064902 (2012).
- [24] A. Darabi, X. Ni, M. Leamy, and A. Alù, Reconfigurable Floquet elastodynamic topological insulator based on synthetic angular momentum bias, *Sci. Adv.* **6**, eaba8656 (2020).
- [25] A. Darabi, M. Collet, and M. J. Leamy, Experimental realization of a reconfigurable electroacoustic topological insulator, *Proc. Natl. Acad. Sci.* **117**, 16138 (2020).
- [26] S. A. R. Kuchibhatla and M. J. Leamy, Nonadiabatic Shifting of a Topological Interface in an Electroacoustic Su-Schrieffer-Heeger Lattice, *Phys. Rev. Appl.* **18**, 054058 (2022).
- [27] M. D. Fronk, L. Fang, P. Packo, and M. J. Leamy, Elastic wave propagation in weakly nonlinear media and metamaterials: A review of recent developments, *Nonlinear Dyn.* **111**, 10709 (2023).
- [28] G. U. Patil and K. H. Matlack, Review of exploiting nonlinearity in phononic materials to enable nonlinear wave responses, *Acta Mech.* **233**, 1 (2022).
- [29] O. R. Bilal, A. Foehr, and C. Daraio, Bistable metamaterial for switching and cascading elastic vibrations, *Proc. Natl. Acad. Sci.* **114**, 4603 (2017).
- [30] G. Trainiti, J. J. Rimoli, and M. Ruzzene, Wave propagation in undulated structural lattices, *Int. J. Solids Struct.* **97**, 431 (2016).
- [31] M. J. Frazier and D. M. Kochmann, Band gap transmission in periodic bistable mechanical systems, *J. Sound Vib.* **388**, 315 (2017).
- [32] Z. Wu, Y. Zheng, and K. W. Wang, Metastable modular metastructures for on-demand reconfiguration of band structures and nonreciprocal wave propagation, *Phys. Rev. E* **97**, 022209 (2018).
- [33] P. Wang, F. Casadei, S. Shan, J. C. Weaver, and K. Bertoldi, Harnessing Buckling to Design Tunable Locally Resonant Acoustic Metamaterials, *Phys. Rev. Lett.* **113**, 014301 (2014).
- [34] S. Li, B. Deng, A. Grinthal, A. Schneider-Yamamura, J. Kang, R. S. Martens, C. T. Zhang, J. Li, S. Yu, and K. Bertoldi, *et al.*, Liquid-induced topological transformations of cellular microstructures, *Nature* **592**, 386 (2021).
- [35] L. Fang, A. Mojahed, A. Darabi, A. F. Vakakis, and M. J. Leamy, Passive Nonreciprocity in a System of Asymmetrical Rotational Oscillators, *Phys. Rev. Appl.* **15**, 034005 (2021).

- [36] L. Fang and M. J. Leamy, Negative Refraction in Mechanical Rotator Lattices, *Phys. Rev. Appl.* **18**, 064058 (2022).
- [37] Y. Chen, X. Li, H. Nassar, G. Hu, and G. Huang, A programmable metasurface for real time control of broadband elastic rays, *Smart Mater. Struct.* **27**, 115011 (2018).
- [38] J. Santini and E. Riva, Elastic temporal waveguiding, *New J. Phys.* **25**, 013031 (2022).
- [39] M. I. Hussein, M. J. Leamy, and M. Ruzzene, Dynamics of phononic materials and structures: Historical origins, recent progress, and future outlook, *Appl. Mech. Rev.* **66**, 040802 (2014).
- [40] L. I. Manevitch and A. F. Vakakis, Nonlinear oscillatory acoustic vacuum, *SIAM J. Appl. Math.* **74**, 1742 (2014).
- [41] M. A. Slawinski, R. A. Slawinski, R. J. Brown, and J. M. Parkin, A generalized form of Snell's law in anisotropic media, *Geophysics* **65**, 632 (2000).
- [42] I. Gandhi and H. Zhou, Synthesizing constant torque compliant mechanisms using precompressed beams, *J. Mech. Des.* **141**, 00 (2019).
- [43] K. P. Jackson, S. A. Newton, B. Moslehi, M. Tur, C. C. Cutler, J. W. Goodman, and H. Shaw, Optical fiber delay-line signal processing, *IEEE Trans. Microw. Theory Tech.* **33**, 193 (1985).
- [44] A. Sharma, V. Kohar, M. D. Shrimali, and S. Sinha, Realizing logic gates with time-delayed synthetic genetic networks, *Nonlinear Dyn.* **76**, 431 (2014).
- [45] J. Vila, R. K. Pal, M. Ruzzene, and G. Trainiti, A Bloch-based procedure for dispersion analysis of lattices with periodic time-varying properties, *J. Sound Vib.* **406**, 363 (2017).
- [46] V. Bolotin, The dynamic stability of elastic systems, *Am. J. Phys.* **33**, 752 (1965).
- [47] T. T. Koutserimpas, A. Alù, and R. Fleury, Parametric amplification and bidirectional invisibility in \mathcal{PT} -symmetric time-Floquet systems, *Phys. Rev. A* **97**, 013839 (2018).
- [48] A. H. Nayfeh and D. T. Mook, *Nonlinear Oscillations* (Wiley, Weinheim, 2004).